Materials Advances

ROYAL SOCIETY OF CHEMISTRY

PAPER

View Article Online
View Journal | View Issue

Cite this: *Mater. Adv.*, 2020, 1, 206

Highly microporous $SbPO_4/BC_x$ hybrid anodes for sodium-ion batteries†

Huiqi Wang, *[a] Li Gou,[a] Weifeng Jing,[a] Duo An,[a] Ying Li,[a] Mei Wang,[a] Ning Li,[a] Shengliang Hu *[a] and Yan-Bing He *[b]

Received 13th February 2020,
Accepted 1st April 2020

DOI: 10.1039/d0ma00024h

rsc.li/materials-advances

The current anode materials greatly restrict the electrochemical performance of sodium-ion batteries. Herein, we propose a highly microporous $SbPO_4/BC_x$ hybrid anode for sodium-ion batteries, exhibiting a high initial reversible capacity of 871 mA h g^{-1} at 50 mA g^{-1}, a good rate capability of around 300 mA h g^{-1} even at 5 A g^{-1} as well as an excellent cycling stability of 500 cycles. The excellent rate capability and cyclability with high capacity are probably due to the novel BC_x structure and stable PO_4^{3-} anions. The abundant micropores serve as reservoirs for storing the sodium ions and shorten the diffusion distance. The high surface area contributes to ample contact area between the electrode and electrolyte, thus achieving a rapid charge-transfer reaction. XPS analysis reveals that the BC_x matrix consists of three B/C structures of BC_3, BC_2O, and BCO_2, and contains around 12.93 at% substitutional boron. Since valence band holes are created by the B/C structures, more sodium ions would be captured easily, which motivates more sodium ions to intercalate electrochemically. Additionally, both the robust BC_x matrix and stable PO_4^{3-} anions as buffers could accommodate the volumetric expansion during the sodium ion insertion, thus optimizing the cycling performance. The strong attachment between $SbPO_4$ and the BC_x matrix would benefit mutual charge transfer between them and keep the integrity of the electrode during the sodiation/desodiation processes, which are favorable for sodium-ion transport and play a crucial role in enhancing the rate performance. Accordingly, the $SbPO_4/BC_x$ composite is expected to become a promising anode for advanced SIBs.

1. Introduction

With regard to large-scale energy storage systems, sodium-ion batteries (SIBs) have gained extensive attention as potential alternatives to lithium-ion batteries (LIBs) due to the natural abundance and low cost of sodium and similar principles to LIBs.[1–5] Currently, the largest challenge of SIBs for practical applications is exploiting suitable electrode materials that can absorb/release sodium ions with enough reversible capacity and diffusion kinetics.[6,7] SIBs are not as attractive as LIBs, mostly because of the lack of anode materials with comparable performance to graphite anodes in LIBs. Among the current anode materials for SIBs, an alloy-type Sb anode is a promising candidate to enable high capacity (660 mA h g^{-1}, Na_3Sb),[1,8] high electronic conductivity, and considerably safe operating potential (0.6 V *vs.* Na^+/Na).[9,10] However, metallic Sb anodes are often subjected to large volume changes (390%) upon cycling,[11–13] which would easily lead to rapid capacity decay.

To alleviate the large volume changes upon cycling of the Sb anodes, carbon buffer was proposed and various composites, such as Sb/hard carbon,[13–18] Sb/carbon black,[11] Sb/carbon fibers,[19] Sb/carbon nanotubes,[20] and Sb/graphene,[7,21–24] have been reported. These carbon matrices, especially hard carbon, also contribute to the sodium storage capacity of about 300 mA h g^{-1},[25–27] yet more than 0.5 times capacity of the carbon matrix was obtained at a low plateau (0.1 V *vs.* Na/Na^+), further triggering security issues during the fast charging processes.[21,27,28] Additionally, the carbon matrix suffers from slow ion diffusion kinetics.[29,30] These deficiencies of metallic Sb anodes and the carbon matrix thus severely hamper their practical applications in SIBs, which urges the exploitation of novel and robust anode materials for SIBs. Recently, layered-structure $SbPO_4$ was explored, for the first time, by Qian *et.al.*,[7] exhibiting hopeful potential as an anode material for SIBs, because bulky and stable PO_4^{3-} anions can buffer the volume change upon cycling and facilitate the cycling stability. Also, Na_3PO_4 generated by the discharge reaction, as an ionic conductor, may reduce the diffusion barrier of sodium ions and promote the

[a] School of Materials Science and Engineering & School of Energy and Power Engineering, North University of China, Taiyuan 030051, P. R. China. E-mail: hqiwang@163.com, hsliang@yeah.net
[b] Shenzhen Geim Graphene Center, Tsinghua Shenzhen International Graduate School, Tsinghua University, Shenzhen, 518055, P. R. China. E-mail: he.yanbing@sz.tsinghua.edu.cn

† Electronic supplementary information (ESI) available. See DOI: 10.1039/d0ma00024h

reaction kinetics. Accordingly, if the conversion of Sb to $SbPO_4$ over the Sb/C anode material was achieved, it would greatly improve the electrochemical performances of pristine metallic Sb anodes. On the other hand, the heteroatom doping and structure engineering of carbon is beneficial to increasing the sodium storage capacity of Sb/C anodes at the expense of the initial Coulombic efficiency and cycling stability.[31–34] Most typically, some documents[35–38] were aimed at the novel graphite-like BC_3 structure as an anode material for alkali metal ion batteries. Many simulation results[35,39] suggest that sodium could effectively intercalate this structure with the maximum sodium concentration, and the much lower potential barrier of BC_3 promotes the sodium transportation, which is helpful in increasing the diffusion rates of sodium atoms inside the BC_3 structure. Thus, these excellent features of BC_3 encourage further experimental studies that the BC_3 structure was used to prepare the volume buffer of the Sb anodes.

Herein, we propose the preparation of $SbPO_4/BC_x$ hybrid anodes for sodium-ion batteries by a facile conversion of Sb to $SbPO_4$ through one-step annealing of a solid mixed powder of Sb/BC_x and $NH_4H_2PO_4$, in which the Sb/BC_x composites were fabricated by pyrolyzing antimony acetate impregnated ammonium pentaborate/starch xerogels at 800 °C under an argon atmosphere. The $SbPO_4/BC_x$ hybrid electrode could provide stable PO_4^{3-} anions and sufficient void space from the BC_x matrix, which can perfectly accommodate the volumetric expansion during the sodium ion insertion, and preserve the structural stability of anodes. As a result, the $SbPO_4/BC_x$ composite as an anode of SIBs exhibits a high initial reversible capacity of 871 mA h g^{-1} at 50 mA g^{-1}, a good rate capability of around 300 mA h g^{-1} even at 5 A g^{-1} and an excellent cycling stability of 500 cycles. Hence, the $SbPO_4/BC_x$ composite is expected to have promising application in future high-performance SIBs.

2. Material and methods

2.1. Material preparation

The Sb/BC_x composite was first synthesized by pyrolyzing antimony acetate impregnated ammonium pentaborate/starch xerogels (Fig. 1). Briefly, 0.7 g of $Sb(CH_3COO)_3$ and 0.15 g of $NH_4B_5O_8$ were dissolved in turn in 20 mL of deionized water. Next, 0.3 g of soluble starch was added to form a white solution. The mixed solution was heated at 85 °C for 1 h under vigorous stirring to obtain a transparent hydrogel. After freeze-drying, the resultant xerogels were carbonized at 800 °C for 2 h under an argon atmosphere, forming the Sb/BC_x composites (denoted as Sb/BC_x). The Sb/C composites and Sb were prepared using a similar method, respectively, and used as the control sample. Afterwards, 0.5 g of the as-prepared Sb/BC_x was fully mixed with 5 g of NaH_2PO_4 powder through hand-grinding, and then the mixture was heated to 400 °C at a rate of 10 °C min^{-1}, and annealed for 1 h in a H_2/Ar (5 : 95) atmosphere. The calcined products were washed with deionized water and alcohol a few times, and dried at 60 °C (denoted as $SbPO_4/BC_x$).

2.2. Structural characterization

X-ray diffraction (XRD) of all the samples was performed on a Bruker AXS D8 with Cu-Kα as a radiation source (λ = 1.5406 Å). Raman spectra were obtained on inVia instrument (Renishaw) with a 532 nm Ar-ion laser as an excitation source. Their morphologies and microstructure were analysed by scanning electron microscopy (SEM, S4800, Hitachi) and transmission electron microscopy (TEM, FEI Tecnai G20). X-ray photoelectron spectroscopy (XPS) was determined on a Thermo spectrometer using Al-Kα radiation (Thermo Scientific, ESCALAN 250Xi). N_2 sorption isotherms were performed on a gas sorptometer at 77 K (Micrometrics ASAP 2020 analyser). Fourier transform infrared (FT-IR) spectra were recorded on a Nicolet 6700 FTIR spectrophotometer over the wavenumber range of 4000–500 cm^{-1}.

2.3. Electrochemical measurements

The electrochemical performance of $SbPO_4/BC_x$ as an anode material in SIBs was studied using CR2025-type coin cells. In each test, the working electrode was prepared by mixing 80 wt% active material, 10 wt% acetylene black, and 10 wt% sodium alginate to form a black slurry, which was then coated on a clean copper foil and dried at 60 °C overnight under vacuum conditions. The mass loading of active materials was about 1.0–2.0 mg cm^{-2}. The cells were assembled in an Ar-filled glove box (MIKROUNA, O_2 < 1 ppm, H_2O < 1 ppm) with sodium foil as the reference and counter electrodes, 1 M $NaClO_6$ solution in EC/DEC (1 : 1 by volume) solvent with 5% fluoroethylene

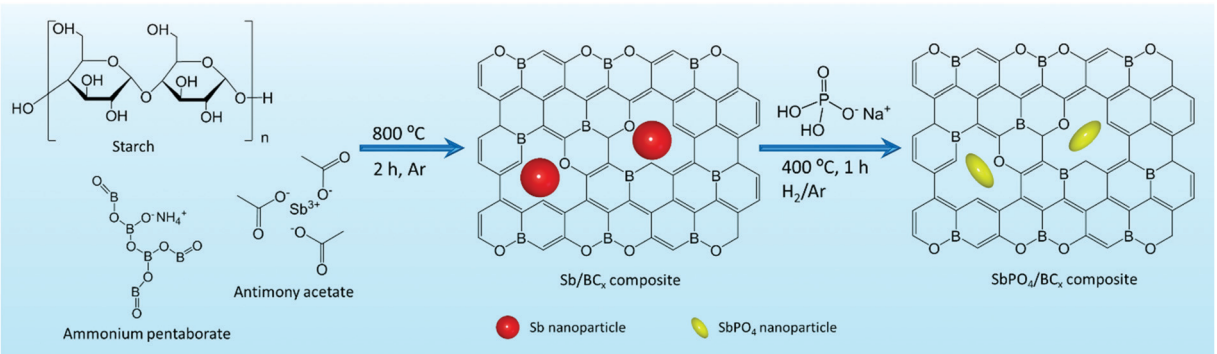

Fig. 1 Schematic illustration of the preparation process for the $SbPO_4/BC_x$ composite.

carbonate as the electrolyte, and the GF/D glass microfiber filter (Whatman) as the separator. Galvanostatic discharge/charge tests were performed on a battery test system (NEWARE CT4008) with a voltage range from 0.01 to 3.0 V. All the capacity values were determined based on the total weight of the active material in the working electrodes. Cyclic voltammetry (CV) was carried out with coin cells at a scan rate of 0.1 mV s^{-1} using a CHI 760E electrochemical workstation. Electrochemical impedance spectroscopy (EIS) of coin cells was performed using an SP200 electrochemical workstation in the frequency range of 10^{-2}-10^{5} Hz by applying an AC voltage of 1 mV amplitude. The Nyquist curves are fitted by Zview software. All the tests were performed at room temperature.

3. Results and discussion

The $SbPO_4/BC_x$ composite was prepared by a solid-phase annealing process (Fig. 1). The morphological characteristics of the precursor Sb/BC_x after pyrolysis at 800 °C under an argon atmosphere are shown in Fig. 2. The spherical Sb nanoparticles with a mean size of 22 nm are uniformly anchored within the BC_x matrix as presented by TEM images (Fig. 2a and b). The HRTEM image in Fig. 2c reveals clear lattice fringes with a *d*-spacing of around 0.31 nm corresponding to the (021) lattice planes of hexagonal Sb. For comparison, the TEM images of the Sb/C composite are shown in Fig. 2d and e, where the Sb nanoparticles with a mean size of 24 nm are unevenly embedded within the carbon matrix, and some cavities can be clearly seen since some Sb nanoparticles are shed from the carbon matrix, in contrast to the Sb nanoparticles in the Sb/BC_x composite that are attached closely to the BC_x matrix. Besides, the HRTEM image of Fig. 2f presents lattice fringes with a *d*-spacing of around 0.31 nm corresponding to the (021) lattice plane for hexagonal Sb, which is consistent with the results from the HRTEM image of the Sb/BC_x composite. The distribution of Sb in the BC_x matrix was confirmed by a scanning transmission electron microscopy (STEM) image, where Sb is identified as white nanodots. The TEM-EDS elemental mappings of Sb, C, B and O correspond to the area shown in Fig. 2g, and the four elements are uniformly distributed over the entire sample. The presence of the O element may be due to the highly porous structure of the Sb/BC_x composite, which can easily absorb oxygen from air on the surface of the material.

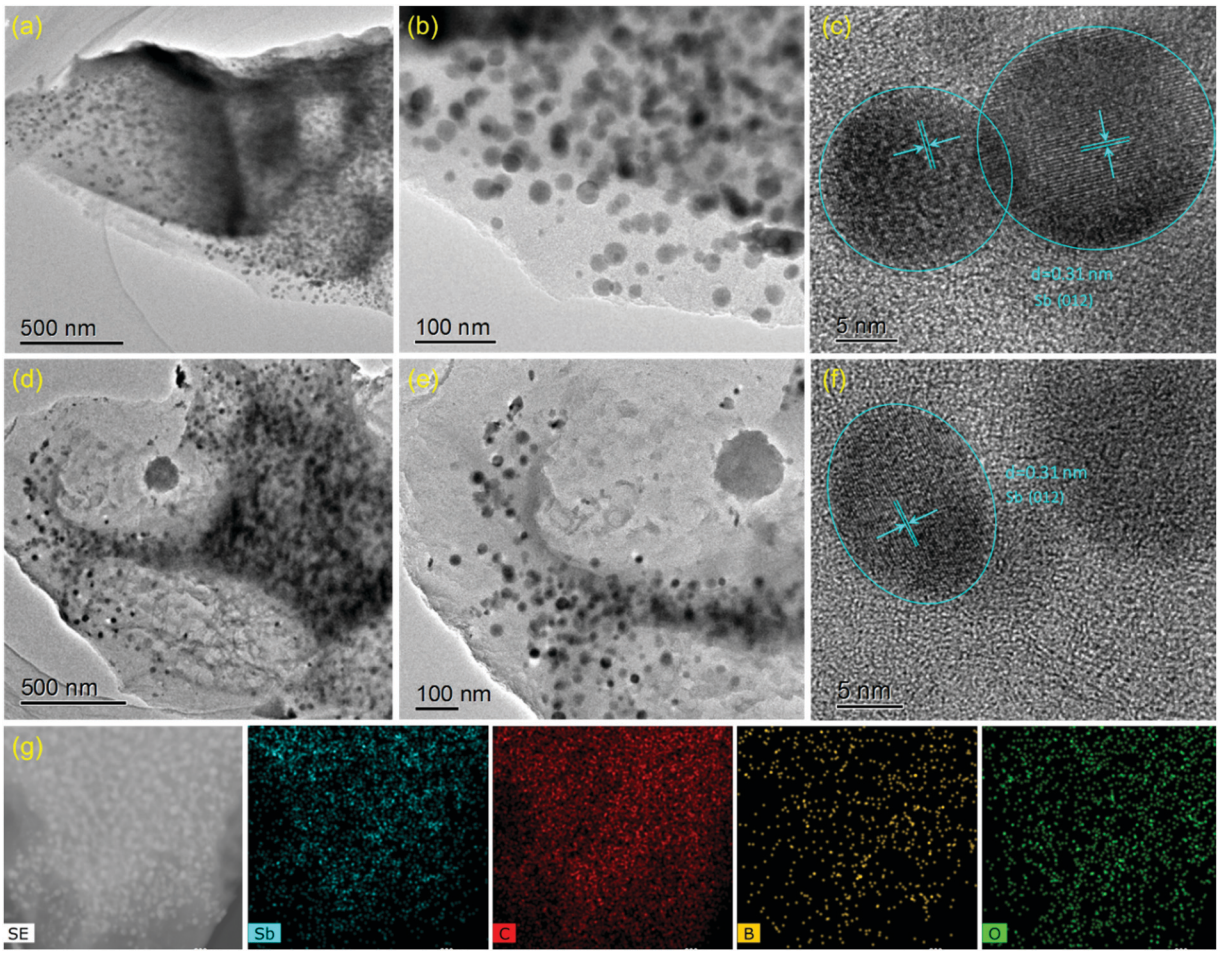

Fig. 2 TEM images (a and b) and HRTEM images (c) of the Sb/ BC_x composite; TEM images (d and e) and HRTEM images (f) of the Sb/C composite; (g) scanning TEM image with its corresponding EDS mappings of the Sb, C, B and O elements for the Sb/BC_x composite.

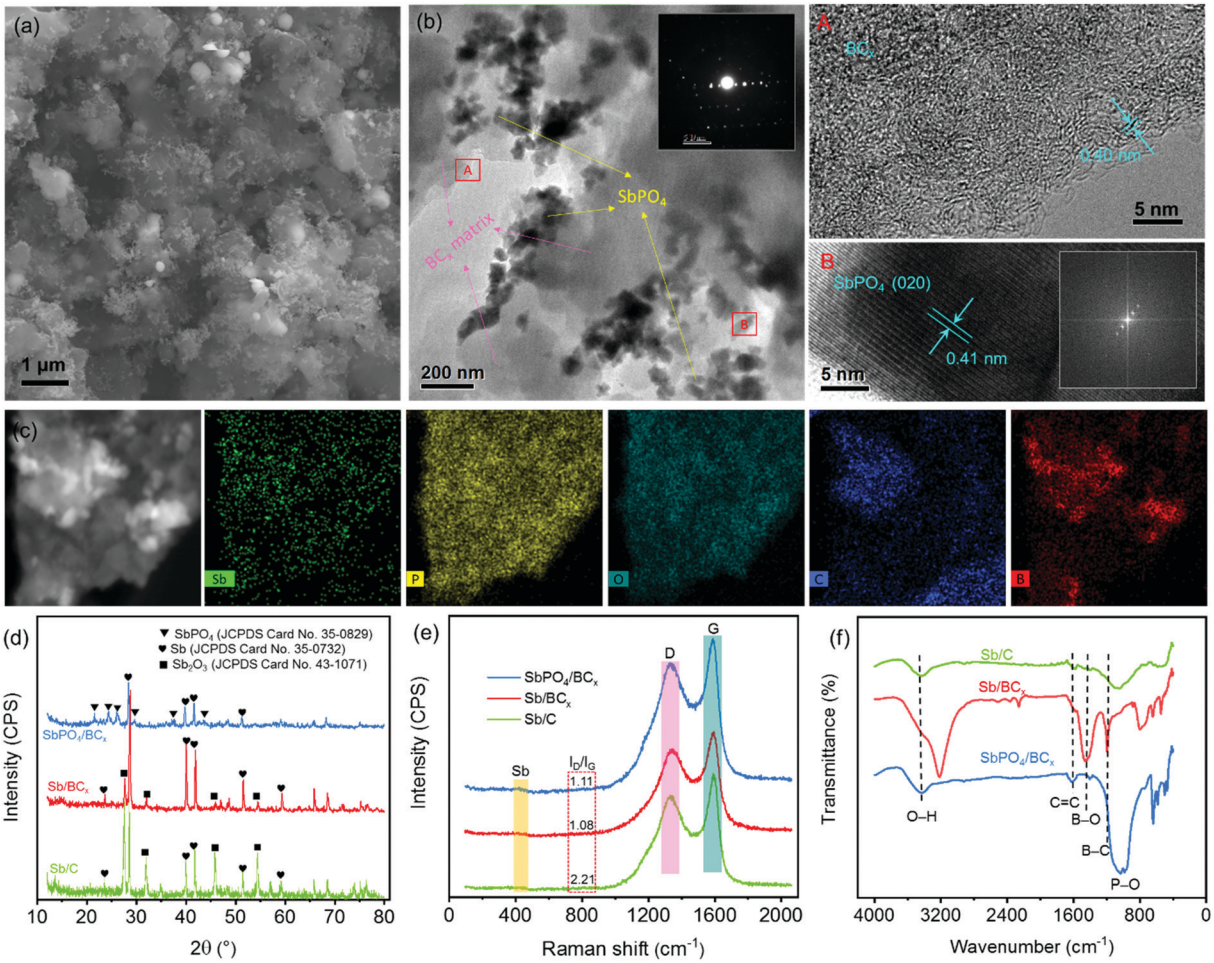

Fig. 3 SEM image (a), TEM and HRTEM images (b), and scanning TEM image with the corresponding EDS mappings of the Sb, P, O, C and B elements (c) of the $SbPO_4/BC_x$ composite; (d) XRD patterns, (e) Raman spectra and (f) FT-IR spectra of the $SbPO_4/BC_x$, Sb/BC_x and Sb/C samples. The two insets present the SAED pattern and the FFT pattern of the HRTEM image.

The characteristics of the $SbPO_4/BC_x$ composite formed by one-step annealing of the solid powder of Sb/BC_x and $NH_4H_2PO_4$ are shown in Fig. 3. The SEM image in Fig. 3a reveals that the $SbPO_4$ nanoparticles are randomly dispersed on the BC_x matrix. The TEM image in Fig. 3b also indicates that there are numerous short rod-like nanoparticles with a diameter of about 50 nm and a length of up to 100 nm. Also, there are a small number of spindles in the $SbPO_4/BC_x$ composite. The selected area electron diffraction (SAED) and the corresponding fast Fourier transform (FFT) patterns (the inset of Fig. 3b) can be indexed to monoclinic $SbPO_4$,[40,41] indicating the presence of a pure phase of $SbPO_4$ in the material. The lattice-resolved HRTEM image of a single nanoparticle in Fig. 3b shows clear lattice fringes with a *d*-spacing of 0.41 nm, assigned to the (020) planes of $SbPO_4$.[7] In the HRTEM image of the BC_x matrix, no obvious long-range-order structure exists, suggesting the amorphous nature of the material. A large number of defects and pores are distributed within the BC_x matrix. The STEM image of the $SbPO_4/BC_x$ composite and the corresponding TEM-EDS element mappings display the good distribution of the Sb, P, O, C and B elements in the material (Fig. 3c). All the above results confirm that the $SbPO_4$ nanoparticles adhere well to the BC_x matrix. The strong attachment would benefit the charge transfer between $SbPO_4$ and the BC_x matrix and retain the integrity of the electrode upon cycling, thereby improving the cycling stability and rate capability.[14,15,25] The XRD patterns in Fig. 3d confirm the phase constituents of the material during each stage of the preparation of the $SbPO_4/BC_x$ composite. The precursor Sb/BC_x displays two phases consisting of Sb (JCPDS Card No. 85-1322) and Sb_2O_3 (JCPDS Card No. 43-1071). Compared with the Sb/C sample, a majority of the Sb_2O_3 phase in Sb/BC_x is reduced to form metallic Sb after doping boron into the carbon matrix, since boron atoms can boost the carbon graphitization process, which largely accelerates the conversion from Sb_2O_3 to Sb. The resultant $SbPO_4/BC_x$ composite displays multiphase components assigned to $SbPO_4$ (JCPDS Card No. 78-1791) and Sb (JCPDS Card No. 85-1322). In addition to the six diffraction peaks of $SbPO_4$ at 21.5°, 24.3°, 26.1°, 29.6°, 37.5° and 43.7°, it shows the diffraction peaks of Sb at 28.6°, 40.1°, 41.8°, and 51.6°. Additionally, no impurity peaks were detected, indicating that the Sb_2O_3 phase was completely converted into the $SbPO_4$ phase. The phase conversion of Sb to $SbPO_4$ can thus

be easily achieved on the BC_x matrix through one-step annealing of the solid mixed powder of Sb/BC_x and $NH_4H_2PO_4$. The ratios of Sb species were obtained by quantitative analysis through the Rietveld refinement of the XRD pattern (Fig. S1, ESI†), and the results are summarized in Table S1 (ESI†). The ratio of Sb to $SbPO_4$ in $SbPO_4/BC_x$ and the ratio of Sb to Sb_2O_3 in Sb/BC_x and Sb/C were about 11.4/88.6, 78.1/21.9, and 28.4/71.6, respectively. The proportion of the Sb phase in $SbPO_4/BC_x$ is much lower than that of the precursor Sb/BC_x, hinting that metallic Sb is also partially converted to $SbPO_4$.

To examine the crystallinity of the BC_x matrix, Raman spectra of the $SbPO_4/BC_x$, Sb/BC_x and Sb/C samples are recorded (Fig. 3e). Except for the peaks around 456 cm^{-1}, corresponding to typical metallic Sb,[25] all the Raman spectra exhibit two prominent peaks at 1340 and 1580 cm^{-1} assigned to the disordered carbon with sp^3 hybridization (D-band) and graphitic carbon with sp^2 hybridization (G-band), respectively.[29,36] The integrated intensity ratio of the D and G bands (I_D/I_G) for the Sb/BC_x composite is 1.08, which is lower than that (2.21) of Sb/C, revealing that the BC_x matrix has a higher graphitization degree.[23,42] In the case of $SbPO_4/BC_x$, the value of I_D/I_G ratio is 1.11, nearly equal to that of Sb/BC_x, suggesting that the phase conversion of Sb to $SbPO_4$ almost does not affect the BC_x structure. FT-IR characterization was also carried out on these samples to elaborate the chemical bonds (Fig. 3f). In all the samples, the broad peak located at ~3445 cm^{-1} was assigned to the O–H stretching vibration, and the peak centered at 1612 cm^{-1} was ascribed to the C=C stretching vibrations. In the $SbPO_4/BC_x$ sample, a prominent feature assigned to P–O stretching vibrations at ~1054 and ~987 cm^{-1} is visible, probably assigned to $SbPO_4$.[40] Except for the Sb/C sample, two extra peaks detected at 1190 and 1410 cm^{-1} in the $SbPO_4/BC_x$ and Sb/BC_x samples were attributed to B–C and B–O stretching vibrations,[43,44] respectively, indicating the successful formation of the BC_x structure by the substitution of boron into the carbon lattice.[45]

X-ray photoelectron spectroscopy (XPS) was conducted to reveal the composition and the chemical bonding states in the $SbPO_4/BC_x$ composite. The signals of Sb, P, O, C and B could be easily detected in the survey spectrum (Fig. 4a). The high-resolution spectra of these elements confirm the existence of the $SbPO_4$ and BC_x structure (Fig. 4b–e). The high-resolution Sb 3d peaks for $SbPO_4/BC_x$ are fitted into four peaks (Fig. 4b), which are assigned to Sb $3d_{5/2}$ (530.3 eV) and Sb $3d_{3/2}$ (539.7 eV) of Sb^{3+}, and Sb $3d_{5/2}$ (528.4 eV) and Sb $3d_{3/2}$ (537.6 eV) of Sb^0, respectively.[6,7] Note that there are two O 1 s peaks located at 532.9 eV and 531.7 eV, which are assigned to the P–O bonding in P_2O_5 and PO_4^{3-}, respectively.[14] For comparison, the high-resolution Sb 3d peaks of Sb/BC_x and Sb/C are also shown (Fig. S2, ESI†). The high-resolution P 2p peaks centered at 134.6 eV for $SbPO_4/BC_x$ are fitted into two peaks (Fig. 4c), which are assigned to P–O (phosphate, 134.3 eV) and P–O (phosphorus oxide, 135.7 eV), respectively.[46,47] These XPS results of Sb 3d and P 2p further confirm that the $SbPO_4/BC_x$ composite consists of $SbPO_4$ and Sb phases, in good accord with the XRD results (Fig. 3d). The high-resolution B 1s peaks for the BC_x matrix are fitted into three peaks (Fig. 4d and Fig. S2, ESI†), corresponding to three B/C structures[36,43] of BC_3 (190.2 eV), BC_2O (191.5 eV), and BCO_2 (193.2 eV), and the other boron

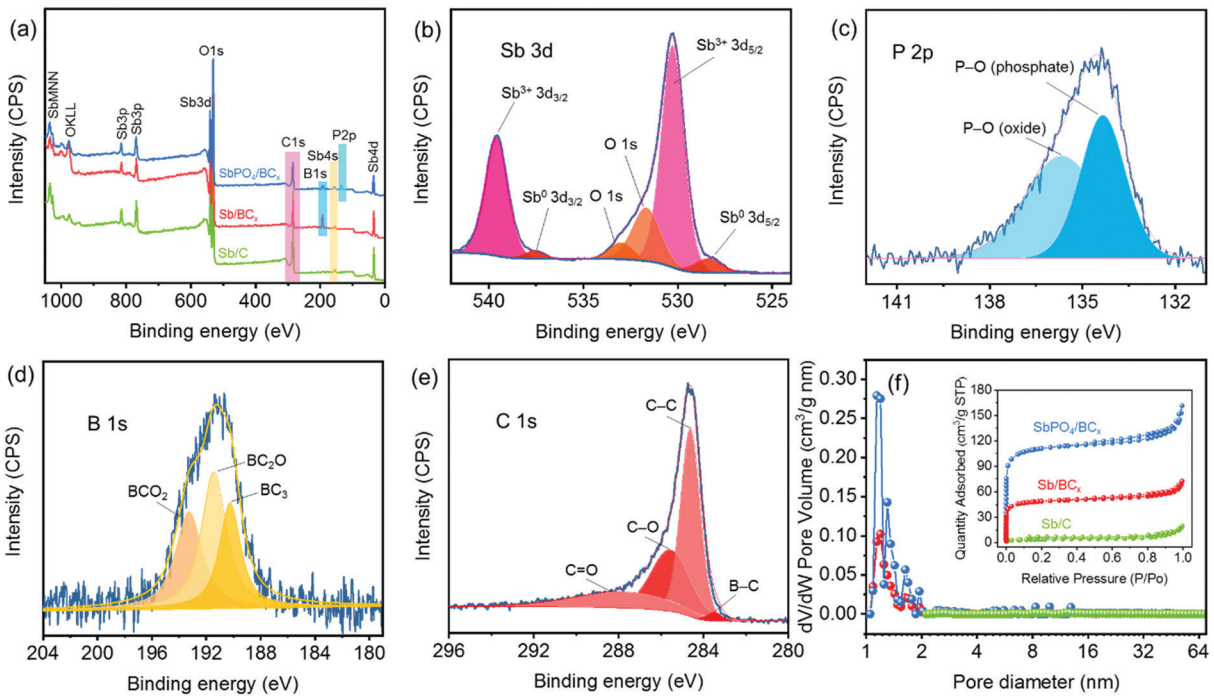

Fig. 4 (a) XPS survey of $SbPO_4/BC_x$, Sb/BC_x and Sb/C, and the fitted Sb 3d signal (b), P 2p signal (c), B 1s signal (d), and C 1 s signal (e) for the $SbPO_4/BC_x$ composite. (f) NLDFT adsorption pore size distribution plots (the inset presents N_2 adsorption–desorption isotherm curves) of the $SbPO_4/BC_x$, Sb/BC_x and Sb/C samples.

species is invisible, suggesting that boron atoms are completely incorporated into the carbon structure. The boron dopant concentrations in the BC_x matrix are obtained through the full XPS spectrum fitting (Table S1, ESI†). The $SbPO_4/BC_x$ composite has a higher boron concentration of 12.93 at%. The ratio of the three B/C structures can thus be determined, and the atomic percentage of BC_3, BC_2O, and BCO_2 is 3.56, 5.28, and 4.10 at%, respectively. These results indicate that more boron atoms replace the carbon atoms at the edge or defect sites of the carbon structure.[43] In all the samples, the C 1s peaks at ~284.6, ~285.6, ~287.8 eV are assigned to C–C, C–O, and C=O, respectively[36,45] (Fig. 3e and Fig. S2, ESI†). The presence of C–O and C=O provides numerous anchoring sites for electrochemically active materials and prevents shedding from the electrodes.[7] Except for Sb/C, the small peak at ~283.5 eV in $SbPO_4/BC_x$ and Sb/BC_x is ascribed to the B–C bonding,[45] revealing that boron atoms are incorporated into the carbon lattice and the formation of the BC_3 structure[43] (Fig. 1). When the graphite-like BC_3 structure was used as the anode material for sodium ion batteries, the sodium ions could effectively intercalate this structure with the maximum concentration, and this unique structure has a much lower potential barrier, which would boost the sodium transportation and create much faster ion diffusion kinetics in the electrode.[35,39]

The microporous characteristics of the $SbPO_4/BC_x$ composite were evaluated through the N_2 adsorption/desorption isotherm analysis (the inset of Fig. 4f). The isotherm curves and the NLDFT model calculation reveal that the $SbPO_4/BC_x$ composite has a highly microporous structure (type-I),[48] centered at approximately 1.2 nm (Fig. 4f), and the microporous structure can also be observed in the HRTEM image of the BC_x matrix (Fig. 3b), which would enable an intimate contact between the electrolyte and electrode upon cycling.[7] These micropores in both $SbPO_4/BC_x$ and Sb/BC_x samples are ascribed to the volatilization of small molecules (the thermal decomposition of $NH_4B_5O_8$) during two-step annealing processes. The surface area was estimated by the BET method and the results are shown in Table S1 (ESI†). Both boron-doping and phase conversion of Sb to $SbPO_4$ greatly increase the BET surface area of the Sb/C composite. The BET surface area of the $SbPO_4/BC_x$ and Sb/BC_x samples sharply increased to 428.24 and 183.92 $m^2\ g^{-1}$, respectively, which is probably due to the structural rearrangement in the porous carbon matrix induced by boron and the phase conversion.[36] This porous structure inhibits the volume expansion of the electrode upon cycling by providing sufficient vacant sites and enables better ion transport through the electrolyte to the active material.[25]

The electrochemical performance of the $SbPO_4/BC_x$ hybrid anode for SIBs was evaluated by cyclic voltammetry (CV), galvanostatic discharge–charge cycling, and electrochemical impedance spectroscopy (EIS). Fig. 3a shows the 1st, 2nd, 3rd and 5th CV curves of the $SbPO_4/BC_x$ electrode at a scan rate of 0.1 mV s^{-1} over 3.0–0.01 V (*vs.* Na^+/Na). The involved electrochemical reaction process upon cycling can be described as eqn (1) and (2):[7]

$$SbPO_4 + 3Na^+ + 3e^- \rightarrow Sb + Na_3PO_4 \quad (1)$$

$$Sb + 3e^- + 3Na^+ \leftrightarrow Na_3Sb \quad (2)$$

In the first sweep, two cathodic peaks at 0.62 and 0.15 V are assigned to the reduction of $SbPO_4$ to metallic Sb and the alloying reaction between Sb and Na, respectively.[40] The anodic peaks at 0.81 and 0.93 V are attributed to the phase transition from the Na_xSb alloy to Sb.[12] In the second sweep, no obvious peaks vanish, implying that the irreversible reactions are greatly inhibited. The cathodic peak at 0.62 V still exists and another peak at 0.42 V appears, which also originates from the generation of a new Na_xSb alloy.[15] The cathodic peak at 0.15 V probably comes from the residual Sb unreacted completely during the first discharge process.[13] Compared to the variations of the cathodic peaks, those of the anodic peaks are invisible. The difference in the CV curves between the first and subsequent cycles is mainly attributed to the formation of the solid electrolyte interphase (SEI) film. The CV curves of the following cycles almost overlap, indicating the good cyclability of the $SbPO_4/BC_x$ electrode. It is noted that correlative plateau regions are observed in the initial five discharge/charge profiles of the $SbPO_4/BC_x$ electrode (Fig. 3b). The first discharge/charge capacity is 756/524 mA h g^{-1}, exhibiting an initial Coulombic efficiency (CE) of 69% at 0.2 A g^{-1}. The low CE value is attributed to the irreversible reactions during the first discharge process, including the generation of the SEI films resulting from the decomposition of the electrolyte, the irreversible sodium-ion insertion into smaller pores, and the irreversible conversion from $SbPO_4$ to metallic Sb.[7] After the initial cycling, the CE value reached 98% at the 3rd cycle and thereafter maintained above 99% after the 5th cycle. Fig. 3c presents the capacity and cycling performance of the $SbPO_4/BC_x$ electrode at 0.2 A g^{-1} in the voltage range of 0.01–3 V (*vs.* Na^+/Na). The $SbPO_4/BC_x$ electrode exhibits much better cycling stability than Sb/BC_x, Sb/C and Sb. After 150 cycles at 0.2 A g^{-1}, the $SbPO_4/BC_x$ electrode shows 78.2% capacity retention and exhibits a reversible capacity of 410 mA h g^{-1}, much higher than 64.5% (270 mA h g^{-1}) of Sb/BC_x, 56.2% (200 mA h g^{-1}) of Sb/C and 4.7% (28 mA h g^{-1}) of Sb, which indicates that the conversion of Sb to $SbPO_4$ over Sb/BC_x induced a sharp increase in sodium storage capacity and enhanced cycling stability, originating from the stable PO_4^{3-} anions as buffers to alleviate the volume change upon cycling. The sodium storage capacity of $SbPO_4/BC_x$ is higher than those of Sb-based anodes reported previously (Table S2, ESI†). These results confirm that the excellent cycling performance of the $SbPO_4/BC_x$ electrode is ascribed to the prominent advantages of the highly microporous structure, the buffer of volume change (stable PO_4^{3-} anions), the lower potential barrier of BC_3, and abundant edge defects[49] (BC_2O, BCO_2).

Fig. 3d shows the superior rate performance of the $SbPO_4/BC_x$ electrode. As the current densities progressively increase from 0.1 to 0.2, 0.5, 1.0, 2.0, and 5.0 A g^{-1}, the electrode exhibits good capacity retention, changing from 440 to 419, 393, 369, 325, and 296 mA h g^{-1}, respectively. When the current density returns stepwise to 2.0, 1.0, 0.5, 0.2 and 0.1 A g^{-1}, capacities of 322, 363, 392, 415 and 430 mA h g^{-1} are obtained, respectively. To give insight into the excellent rate performance of the $SbPO_4/BC_x$ electrode, EIS spectra were collected after 10 cycles and fitted by a Randle-type equivalent circuit model (the inset of Fig. 3e).

Fig. 3e presents the Nyquist plots of the $SbPO_4/BC_x$, Sb/BC_x, Sb/C and Sb electrodes; all the spectra consist of semicircles in the medium–high frequency region and sloping straight lines in the low-frequency region, which are related to the charge-transfer resistance (R_{ct}) and solid-state diffusion of sodium in the electrode material, respectively.[7,20] A shown in Table S3 (ESI†), the $SbPO_4/BC_x$ electrode exhibits the lowest charge-transfer resistance (R_{ct} = 44.43 Ω), which indicates its high electrical conductivity and enhanced reaction kinetics upon cycling. The results obtained from the 4-point probe method further confirm that the electronic conductivity of $SbPO_4/BC_x$ is much larger than those of Sb/BC_x and Sb/C (Table S3, ESI†). The relationship between Z_{re} and $\omega^{-1/2}$ in Fig. 3f represents the Warburg impedance related to sodium-ion diffusion. The $SbPO_4/BC_x$ electrode displays the lowest slope (σ = 9.18) among the three electrodes (Table S3, ESI†), implying facile sodium-ion transportation. The EIS result is consistent with its excellent cycling and rate performance, hinting the reinforced electron and ion transport. These results thus suggest that the robust B/C structure and stable PO_4^{3-} anions are favorable for sodium-ion transport and play an important role in enhancing the rate performance (Fig. 5).

A long-term cycling at a high current rate of 5 A g^{-1} is achieved for the $SbPO_4/BC_x$ electrode (Fig. 6a). After a few activation cycles under 0.2 A g^{-1}, the capacity remains at 300 mA h g^{-1}. In the following cycles, the capacity decreases to 127 mA h g^{-1} after 150 cycles, 118 mA h g^{-1} after 300 cycles, and 112 mA h g^{-1} after 500 cycles. Thus, the $SbPO_4/BC_x$ electrode at a high current rate exhibits the low capacity retention of 37.3% as well as good cycling stability. The large initial capacity fading of $SbPO_4/BC_x$ is probably attributed to the restricted buffering ability to adjust the volume expansion, which can be proved by observing the morphologies of electrodes before and after cycling (Fig. S3, ESI†). After 500 cycles, a small number of cracks are observed on the surface of the $SbPO_4/BC_x$ electrode, which make it hard to retain the integrity of the electrode upon cycling. The TEM images in Fig. 6b show that the BC_x matrix still retains its primary structure after 500 cycles, accounting for the good cycling stability of the $SbPO_4/BC_x$ electrode at a high current rate.

The excellent rate capability and cyclability with high capacity could be illustrated by the robust BC_x structure and stable PO_4^{3-} anions (Fig. 6c). The amorphous BC_x structure with a large *d*-spacing of ~0.41 nm can intercalate more sodium ions. The abundant micropores serve as reservoirs for storing the sodium ions and shorten the diffusion distance. The high S_{BET} value leads to the large contact area between the electrode and electrolyte, thus exhibiting the rapid charge-transfer reaction. Additionally, since valence band holes are created by boron doping, more sodium ions would be captured easily in the BC_x structure, which motivates more sodium ions to intercalate electrochemically. Both the robust BC_x matrix and stable PO_4^{3-} anions as buffers could alleviate the volume change upon cycling, optimizing the cycling performance. The strong attachment between $SbPO_4$ and BC_x matrix would benefit mutual charge transfer between them, and keep the integrity of the electrode during the sodiation/desodiation processes. All of these merits make the $SbPO_4/BC_x$ composite promising as an anode material for SIBs.

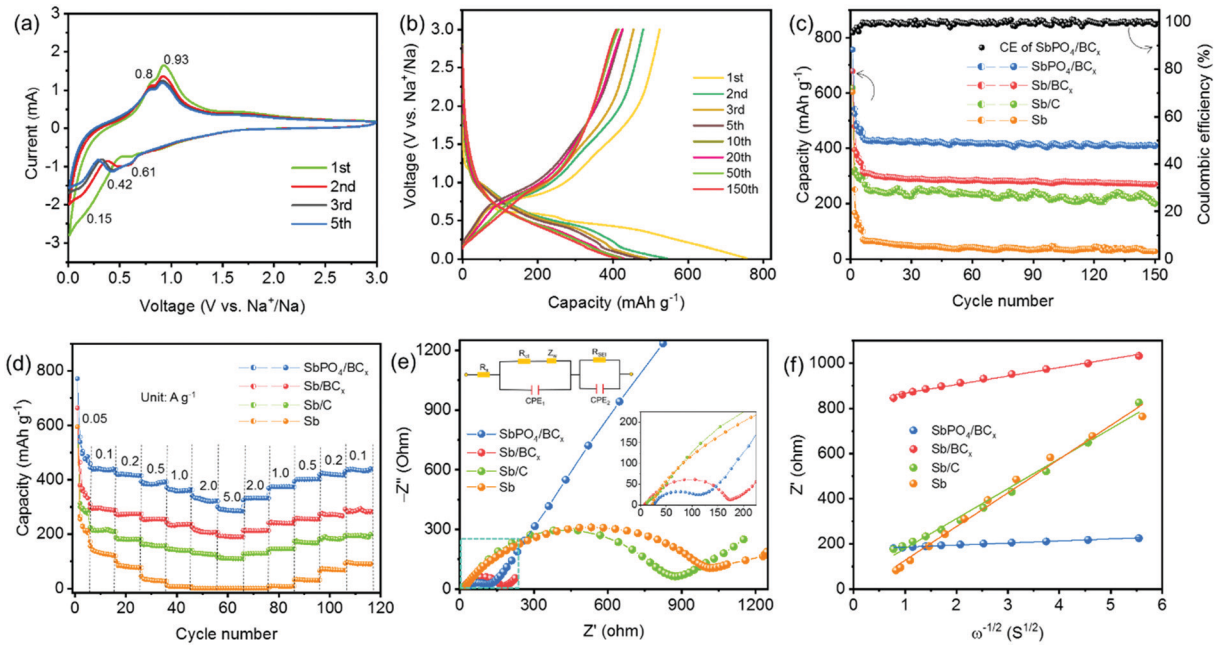

Fig. 5 (a) CV curves of the $SbPO_4/BC_x$ electrode at a scan rate of 0.1 mV s^{-1}. (b) Galvanostatic charging/discharging curves of the $SbPO_4/BC_x$ electrode at a current rate of 0.2 A g^{-1} over 3.0–0.01 V. (c) Cycle performance of the $SbPO_4/BC_x$, Sb/BC_x, Sb/C and Sb electrodes at a current rate of 0.2 A g^{-1} over 3.0–0.01 V. (d) Rate performance of the $SbPO_4/BC_x$, Sb/BC_x, Sb/C and Sb electrodes at various current rates from 0.1 to 5.0 A g^{-1}. Nyquist impedance plots and the magnified area (inset) in the range of 0–225 Ohm (e) and the corresponding relationship between the real part of the impedance (Z_{re}) and $\omega^{-1/2}$ (f) of the $SbPO_4/BC_x$, Sb/BC_x, Sb/C and Sb electrodes.

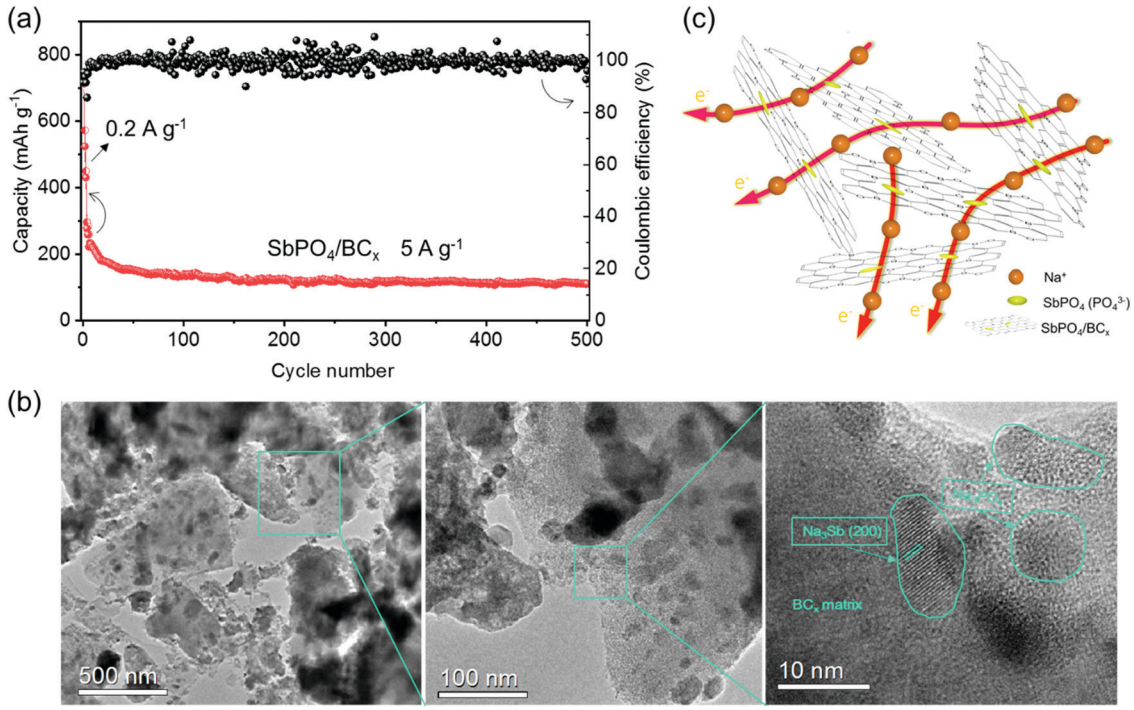

Fig. 6 (a) Cycling performance of the $SbPO_4/BC_x$ electrode at 5 A g^{-1} after three cycles at 0.2 A g^{-1}. (b) TEM images of the $SbPO_4/BC_x$ electrode after 500 cycles. (c) Proposed mechanism of the $SbPO_4/BC_x$ composite during the sodium storage processes.

4. Conclusions

In summary, we propose a $SbPO_4/BC_x$ hybrid anode for sodium-ion batteries by a facile conversion of Sb to $SbPO_4$ through one-step annealing of a solid mixed powder of Sb/BC_x and $NH_4H_2PO_4$, where the Sb/BC_x composites are prepared by pyrolyzing antimony acetate impregnated ammonium pentaborate/starch xerogels under an Ar atmosphere at 800 °C. When used as the anode of SIBs, the $SbPO_4/BC_x$ composite exhibits a high initial reversible capacity of 871 mA h g^{-1} at 50 mA g^{-1}, a good rate capability of about 300 mA h g^{-1} even at 5 A g^{-1} and an excellent cycling stability of 500 cycles. These results confirm that the excellent cycling performance of the $SbPO_4/BC_x$ electrode is ascribed to the prominent advantages of a highly microporous structure, the buffer of volume change (stable PO_4^{3-} anions), the lower potential barrier of BC_3, and abundant edge defects (BC_2O, BCO_2). The novel B/C structure and stable PO_4^{3-} anions are favorable for sodium-ion transport and play an important role in enhancing the rate performance. It is believed that this easy method of combining $SbPO_4$ with a BC_x matrix might be extended to other anode materials for reinforced electrochemical performance of SIBs.

Conflicts of interest

There are no conflicts to declare.

Acknowledgements

This work was financially supported by the National Natural Science Foundation of China (No. 21703209, 51502270, U1510125, 51272301), the Key Research and Development (R&D) Projects of Shanxi Province (No. 201803D121037), the Program for the Outstanding Innovative Teams of Higher Learning Institutions of Shanxi, the Specialized Research Fund for Sanjin Scholars Program of Shanxi Province, and the North University of China Fund for Scientific Innovation Team.

Notes and references

1 W. T. Jing, C. C. Yang and Q. Jiang, *J. Mater. Chem. A*, 2020, **8**, 2913–2933.
2 C. Kudakwashe, M. Grietus, D. L. Danilov and P. H. L. Notten, *Adv. Energy Mater.*, 2018, **8**, 1800079.
3 Y. Fang, L. Xiao, Z. Chen, X. Ai, Y. Cao and H. Yang, *Electrochem. Energy Rev.*, 2018, **1**, 294–323.
4 C. Delmas, *Adv. Energy Mater.*, 2018, **8**, 1703137.
5 Y. Y. Zhou, Y. L. Yang, M. G. Jiao and Z. Zhou, *Sci. Bull.*, 2018, **63**, 146–148.
6 J. Pan, Y. Zhang, L. Li, Z. Cheng, Y. Li, X. Yang, J. Yang and Y. Qian, *Small Methods*, 2019, **3**, 1900231.
7 J. Pan, S. Chen, Q. Fu, Y. Sun, Y. Zhang, N. Lin, P. Gao, J. Yang and Y. Qian, *ACS Nano*, 2018, **12**, 12869–12878.
8 L. Liang, Y. Xu, C. Wang, L. Wen, Y. Fang, Y. Mi, M. Zhou, H. Zhao and Y. Lei, *Energy Environ. Sci.*, 2015, **8**, 2954–2962.
9 Z. Liu, T. Song and U. Paik, *J. Mater. Chem. A*, 2018, **6**, 8159–8193.
10 B. Wang, Z. Deng, Y. Xia, J. Hu, H. Li, H. Wu, Q. Zhang, Y. Zhang, H. Liu and S. Dou, *Adv. Energy Mater.*, 2020, **10**, 1903119.

11 H. Hou, Y. Yang, Y. Zhu, M. Jing, C. Pan, L. Fang, W. Song, X. Yang and X. Ji, *Electrochim. Acta*, 2014, **146**, 328–334.
12 X. Zhou, Y. Zhong, M. Yang, M. Hu, J. Wei and Z. Zhou, *Chem. Commun.*, 2014, **50**, 12888–12891.
13 M. Wang, Z. Yang, J. Wang, W. Li, L. Gu and Y. Yu, *Small*, 2015, **11**, 5381–5387.
14 T. Ramireddy, N. Sharma, T. Xing, Y. Chen, J. Leforestier and A. M. Glushenkov, *ACS Appl. Mater. Interfaces*, 2016, **8**, 30152–30164.
15 J. Duan, W. Zhang, C. Wu, Q. Fan, W. Zhang, X. Hu and Y. Huang, *Nano Energy*, 2015, **16**, 479–487.
16 P. Li, L. Yu, S. Ji, X. Xu, Z. Liu, J. Liu and J. Liu, *Chem. Eng. J.*, 2019, **374**, 502–510.
17 S. Qiu, X. Wu, L. Xiao, X. Ai, H. Yang and Y. Cao, *ACS Appl. Mater. Interfaces*, 2016, **8**, 1337–1343.
18 T. Wu, H. Hou, C. Zhang, P. Ge, Z. Huang, M. Jing, X. Qiu and X. Ji, *ACS Appl. Mater. Interfaces*, 2017, **9**, 26118–26125.
19 H. Hou, M. Jing, Y. Yang, Y. Zhang, W. Song, X. Yang, J. Chen, Q. Chen and X. Ji, *J. Power Sources*, 2015, **284**, 227–235.
20 X. Zhou, Z. Dai, J. Bao and Y.-G. Guo, *J. Mater. Chem. A*, 2013, **1**, 13727–13731.
21 X. Liu, M. Gao, H. Yang, X. Zhong and Y. Yu, *Nano Res.*, 2017, **10**, 4360–4367.
22 L. Li, K. H. Seng, D. Li, Y. Xia, H. K. Liu and Z. Guo, *Nano Res.*, 2014, **7**, 1466–1476.
23 K. Wang, Y. Xu, Y. Li, V. Dravid, J. Wu and Y. Huang, *J. Mater. Chem. A*, 2019, **7**, 3327–3335.
24 Y.-L. Ding, C. Wu, P. Kopold, P. A. van Aken, J. Maier and Y. Yu, *Small*, 2015, **11**, 6026–6035.
25 X.-M. Pham, D. T. Ngo, H. T. T. Le, P. N. Didwal, R. Verma, C.-W. Min, C.-N. Park and C.-J. Park, *Nanoscale*, 2018, **10**, 19399–19408.
26 X. Zhou and Y.-G. Guo, *ChemElectroChem*, 2014, **1**, 83–86.
27 N. Sun, Z. Guan, Y. Liu, Y. Cao, Q. Zhu, H. Liu, Z. Wang, P. Zhang and B. Xu, *Adv. Energy Mater.*, 2019, **9**, 1901351.
28 X. Dou, I. Hasa, D. Saurel, C. Vaalma, L. Wu, D. Buchholz, D. Bresser, S. Komaba and S. Passerini, *Mater. Today*, 2019, **23**, 87–104.
29 H. Hou, X. Qiu, W. Wei, Y. Zhang and X. Ji, *Adv. Energy Mater.*, 2017, **7**, 1602898.
30 Y. Yu, X. Zhong, Y. Wu and S. Zen, *Chem. – Asian J.*, 2018, **13**, 1248–1265.
31 M. Wang, Y. Yang, Z. Yang, L. Gu, Q. Chen and Y. Yu, *J. Adv. Sci.*, 2017, **4**, 1600468.
32 S. Qiu, L. Xiao, M. L. Sushko, K. S. Han, Y. Shao, M. Yan, X. Liang, L. Mai, J. Feng, Y. Cao, X. Ai, H. Yang and J. Liu, *Adv. Energy Mater.*, 2017, **7**, 1700403.
33 H. Chen, Y. Xiong, T. Yu, P. Zhu, X. Yan, Z. Wang and S. Guan, *Carbon*, 2017, **113**, 266–273.
34 D. Ni, W. Sun, Z. Wang, Y. Bai, H. Lei, X. Lai and K. Sun, *Adv. Energy Mater.*, 2019, **9**, 1900036.
35 R. P. Joshi, B. Ozdemir, V. Barone and J. E. Peralta, *J. Phys. Chem. Lett.*, 2015, **6**, 2728–2732.
36 H. Wang, Y. Li, Y. Wang, S. Hu and H. Hou, *J. Mater. Chem. A*, 2017, **5**, 2835–2843.
37 S. Gong and Q. Wang, *J. Phys. Chem. C*, 2017, **121**, 24418–24424.
38 P. Bhauriyal, A. Mahata and B. Pathak, *J. Phys. Chem. C*, 2017, **121**, 9748–9756.
39 A. A. Kuzubov, A. S. Fedorov, N. S. Eliseeva, F. N. Tomilin, P. V. Avramov and D. G. Fedorov, *Phys. Rev. B: Condens. Matter Mater. Phys.*, 2012, **85**, 195415.
40 Y. Wang, L. Li and G. Li, *RSC Adv.*, 2012, **2**, 12999–13006.
41 M. Ou, Y. Ling, L. Ma, Z. Liu, D. Luo and L. Xu, *Mater. Lett.*, 2018, **224**, 100–104.
42 X.-F. Luo, C.-H. Yang, Y.-Y. Peng, N.-W. Pu, M.-D. Ger, C.-T. Hsieh and J.-K. Chang, *J. Mater. Chem. A*, 2015, **3**, 10320–10326.
43 X. Yu, P. Han, Z. Wei, L. Huang, Z. Gu, S. Peng, J. Ma and G. Zheng, *Joule*, 2018, **2**, 1610–1622.
44 S. Wang and X.-B. Zhang, *Adv. Mater.*, 2019, **31**, 1805432.
45 H. Wang, Q. Guo, J. Yang, Z. Liu, Y. Zhao, J. Li, Z. Feng and L. Liu, *Carbon*, 2013, **56**, 296–308.
46 C. Zhang, X. Wang, Q. Liang, X. Liu, Q. Weng, J. Liu, Y. Yang, Z. Dai, K. Ding, Y. Bando, J. Tang and D. Golberg, *Nano Lett.*, 2016, **16**, 2054–2060.
47 K. Lu, S. Lu, T. Gu, X. Zheng, K. Ke, X. Li and R. Yang, *Electrochem. Commun.*, 2019, **103**, 22–26.
48 L. Hao, B. Luo, X. Li, M. Jin, Y. Fang, Z. Tang, Y. Jia, M. Liang, A. Thomas, J. Yang and L. Zhi, *Energy Environ. Sci.*, 2012, **5**, 9747–9751.
49 H. Wang, D. An, N. Li, Y. Li, M. Wang, J. Zhang, S. Hu and Y.-B. He, *J. Power Sources*, 2020, **461**, DOI: 10.1016/j.jpowsour.2020.228110.